


Integrated Multichannel Lithium Niobate Waveguides for Quantum Frequency Conversion

Ming-Yang Zheng,¹ Quan Yao,¹ Bin Wang,^{1,2,3} Xiu-Ping Xie,¹ Qiang Zhang[✉],^{1,2,3,*} and Jian-Wei Pan^{2,3,†}

¹Jinan Institute of Quantum Technology, Jinan, Shandong 250101, P. R. China

²Shanghai Branch, National Laboratory for Physical Sciences at Microscale and Department of Modern Physics, University of Science and Technology of China, Shanghai 201315, P. R. China

³Shanghai Branch, CAS Center for Excellence and Synergetic Innovation Center in Quantum Information and Quantum Physics, University of Science and Technology of China, Shanghai 201315, P. R. China

 (Received 22 May 2020; revised 2 July 2020; accepted 22 July 2020; published 14 September 2020)

In this paper, we demonstrate integrated photonic chips for multichannel quantum frequency conversion (QFC) based on reverse-proton-exchange periodically poled lithium niobate waveguides. The integrated chip is fiber coupled with two 34-channel fiber arrays, showing an average fiber-to-fiber sum-frequency generation (SFG) conversion efficiency of about 60% for multichannels. Then the same integrated chip is used to perform multichannel differential-frequency generation (DFG), showing the potential application in long-distance multimode quantum memory. Moreover, the integrated chip is utilized to construct a multichannel up-conversion detector, which has extensive applications including deep-space laser communication, high-rate quantum-key distribution, and single-photon imaging.

DOI: [10.1103/PhysRevApplied.14.034035](https://doi.org/10.1103/PhysRevApplied.14.034035)

I. INTRODUCTION

Quantum frequency conversion (QFC), an efficient nonlinear process to convert the frequency of light at single-photon level while preserving its quantum statistics [1,2], has found wide applications in quantum information research. First, it has been found that an infrared single photon can be up converted to the visible band and detected by using a commercial silicon avalanche photodiode (APD) with high efficiency and a low noise count rate [3–10], thereby extending the operating spectra range of silicon APDs. Moreover, the connection of quantum memory over a long distance using low-loss transmission in fiber can be realized by shifting the wavelength of the visible-band single photon emitted from the quantum memory to the telecommunication band [11–16]. Furthermore, the frequency distinguishability of two single photons can be erased by QFC, which can be used to establish a color-erasure single-photon detector [17,18]. In these previous experiments, highly efficient QFCs have been implemented with periodically poled lithium niobate (PPLN) waveguides, benefiting from strong optical confinement in the material with a wide transparency window (350–4500 nm), a large optical nonlinearity efficient, and flexible ferroelectric domain control. However, all reported

quantum frequency converters have been using single-channel frequency mixing, which cannot satisfy the needs of emerging applications, including single-photon level imaging [19–21] and quantum interfaces for multimode quantum memories [22–28].

In this work, we exploit the mature reverse-proton-exchange (RPE) PPLN waveguide technique to fabricate monolithic chips for multichannel QFCs [3,5,7,8], which are designed for multichannel 1550-nm/1950-nm sum-frequency generation (SFG). We therefore report an instance of integrated multichannel QFCs. In order to show its applications, we first demonstrate multichannel DFGs converting 863-nm light into the 1550-nm telecom band, which may find immediate applications in quantum interfaces between multimode quantum memory and deployed optical-fiber infrastructure. Moreover, we build a multichannel up-conversion single-photon detector (SPD) array for 1550-nm light with the integrated chip, which may have extensive applications in deep-space laser communication, high-rate quantum-key distribution, and single-photon imaging.

II. FABRICATION AND CHARACTERIZATION

Photographs of the packaged 34-channel integrated chip and a microscopic image of the waveguides are shown in Fig. 1. The 52-mm-long and 5.5-mm-wide multichannel PPLN waveguide device, cut from a 0.5-mm-thick wafer, is composed of 34 adjacent independent-channel

*qiangzh@ustc.edu.cn

†pan@ustc.edu.cn

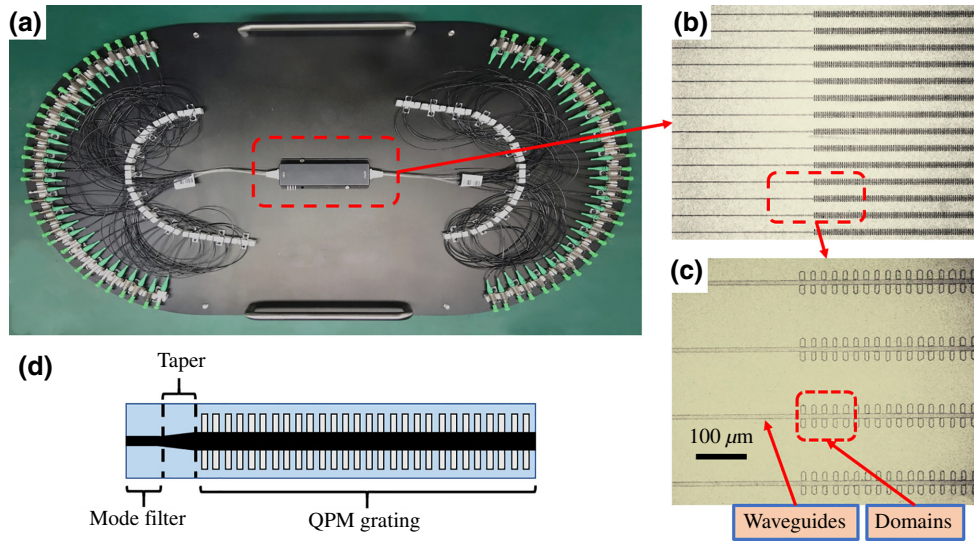


FIG. 1. (a) A photograph of a packaged PPLN waveguide chip with a 34-channel input and output fiber couplings. (b) A microscopic image of a multichannel waveguide chip. (c) Details of the microstructure on the chip, with a higher magnification of $200\times$. The chip shown in (b) and (c) is of the same design and processing as the packaged one in (a) and has been etched using hydrofluoric acid to reveal the waveguides and poling domains. (d) A schematic of the single-channel waveguide structure.

waveguides with the same design parameters. The total length of each channel waveguide is 52 mm, including the mode filter, the taper, and the straight waveguide with quasi-phase-matching (QPM) gratings [8]. A 1-mm-long $3.5\text{-}\mu\text{m}$ wide mode filter is located at the input port of the waveguide, followed by a 1-mm-long linear taper, with the waveguide width increasing from $3.5\ \mu\text{m}$ to $8.0\ \mu\text{m}$, the latter value being maintained through the remaining waveguide. The grating length is 48 mm, with a poling period of $20\ \mu\text{m}$. A polarization-maintaining (PM) fiber array consisting of 34 pieces of 1550-nm PM single-mode fiber with a core spacing of $127\ \mu\text{m}$ is used for input coupling. To ensure high and uniform coupling efficiencies between the PM fibers and the waveguides, the horizontal concentric axial spacing errors of the 34 fiber cores are required to be $< 0.5\ \mu\text{m}$. A multimode fiber array is used for output coupling and is composed of 34-channel multimode fibers. Both the input and output end facets of the PPLN waveguide are antireflection coated to eliminate the Fresnel reflection loss.

To measure the performance of the individual channels in the integrated device [7], the 1950-nm pump beam is combined with the 1550-nm signal via 1550-nm/1950-nm wavelength-division multiplexing (WDM) and then launched into the fiber array at the input port. The fibers in all the optical components, including the lasers and the WDM, are polarization maintaining because the PPLN waveguide is fabricated using the RPE method and thus guides only the transverse-magnetic (TM) modes. The working temperature of the chip is controlled by a thermoelectric cooling (TEC) system to maintain the phase-matching condition. The SFG signal at the 863-nm band,

along with the residual 1550-nm signal and the 1950-nm pump, are then coupled into the multimode fiber array at the output port. The phase-matching wavelengths and conversion efficiencies of the 34-channel waveguides are measured. The typical curves are shown in Fig. 2.

As shown in Fig. 2(a), the SFG tuning curve of the 16th channel waveguide is obtained by sweeping the signal wavelength around 1550 nm with the pump wavelength fixed at 1950 nm. The phase-matching signal wavelength of the selected waveguide is 1550.4 nm at a room temperature of around $25\ ^\circ\text{C}$, with a full width at half maximum (FWHM) of 0.65 nm.

The signal-photon conversion efficiency η is

$$\eta = \frac{P_{\text{SFG}}\lambda_{\text{SFG}}}{P_{\text{Signal}}\lambda_{\text{Signal}}}, \quad (1)$$

where λ_{SFG} and λ_{Signal} are the SFG and signal wavelengths, P_{SFG} is the SFG power at the output port of the waveguide, and P_{Signal} is the signal power at the input port of the waveguide, which is fixed at 2 mW in the measurements.

Figure 2(b) shows the conversion efficiencies versus the pump power measured at the output port of the 16th channel waveguide. As illustrated, the signal-photon conversion efficiency of the waveguide reaches its maximum when the pump power is 92 mW, corresponding to a normalized conversion efficiency η_{nor} of $116.3\%/(\text{W cm}^2)$, which is calculated with [3,5]

$$\eta_{\text{nor}} = \frac{\pi^2}{4L^2P_{\text{max}}}, \quad (2)$$

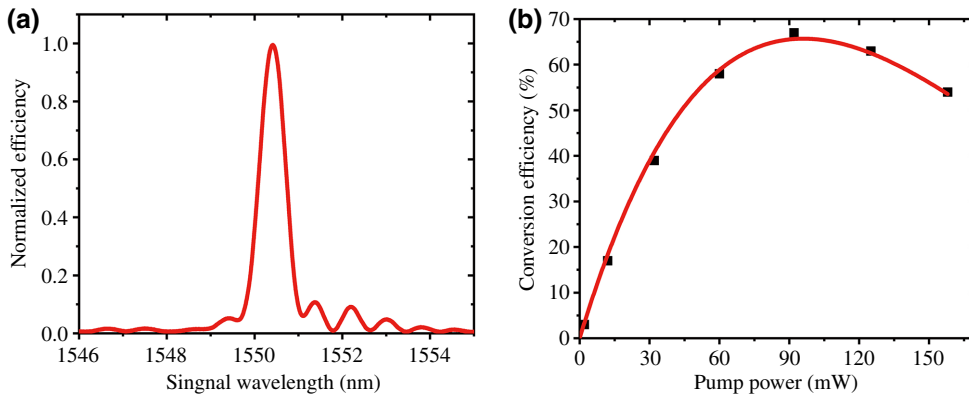


FIG. 2. (a) The SFG tuning curve, (b) The measured SFG conversion efficiency versus the pump power (solid square) and the $\sin^2(\cdot)$ fitting curve [3].

where L is the length of the QPM gratings and P_{\max} is the pump power required for maximum conversion.

The signal-photon conversion efficiency of each individual waveguide does not reach 100% due to the propagation loss in the waveguide and the coupling loss at the input port and other devices in the optical path. When the working temperature of the chip is kept at a certain temperature and the conversion efficiency is optimized for one channel waveguide by tuning the signal wavelength, the other channels may perform worse at that optimally tuned signal wavelength. In the following test, the signal and pump wavelengths are set at 1550 nm and 1950 nm, respectively. An optimized working temperature at 23 °C is chosen for obtaining uniform performance over all the channels. The pump power at the maximum-conversion-efficiency point for each channel is a little different due to fabrication errors, including random duty-cycle errors of the QPM gratings and waveguide-width errors, and should be individually optimized accordingly when the integrated chip is used as a whole.

Calculated from the measured SFG power at the maximum conversion points of every channel, the maximum signal-conversion efficiencies for all 34 channels are shown in Fig. 3 using solid square symbols. We find that the conversion efficiencies of the first two and the last two channels are much lower than those for the other 30 channels in the middle. This is mainly attributed to the temperature gradient and liquid turbulence in the fabrication ovens for the proton-exchange and RPE processes. Apart from the four side channels, an average conversion efficiency of about 60% is achieved. The differences over the 30 channels in the middle may be due to fabrication errors, including random duty-cycle errors of the QPM gratings, waveguide-width errors, and the temperature gradient in the fabrication ovens. To increase the number of channels with uniform high conversion efficiencies, we may improve the temperature uniformity of the fabrication ovens or simply decrease the spacing between the waveguide channels, if a fiber array with smaller spacing is available. With a fiber-to-fiber (waveguide center-to-center) spacing of 63 μm , we may easily obtain 60

channels with uniformly high conversion efficiencies. Such an integrated multichannel frequency mixing chip could be utilized to build multichannel SPDs, long-distance quantum fiber networks with multimode quantum memory, and so on.

A multichannel DFG experiment is carried out to demonstrate the potential use of the integrated chip in long-distance multimode quantum memory. The 863-nm signal is combined with the 1950-nm pump via an 863-nm/1950-nm WDM and then launched into the input fibers of the integrated 1550-nm/1950-nm SFG chip and the DFG output is measured for each channel. An average down-conversion efficiency of 23% over the middle 30 channels is shown in Fig. 3 using hollow square symbols. We observe a significant decrease of efficiency of approximately 60% mainly due to the fiber-waveguide coupling loss at the input port, where a large proportion of the signal power is coupled to high-order TM modes and cannot be down converted. However, the DFG conversion efficiency could be as high as the SFG conversion

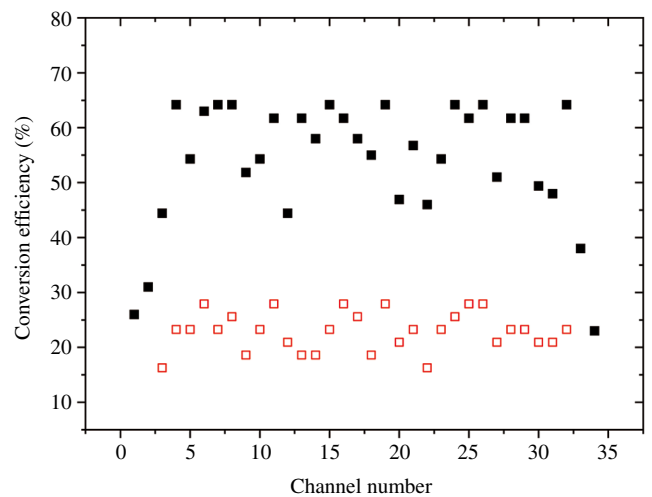


FIG. 3. The measured SFG (solid square) and DFG (hollow square) conversion efficiencies versus the waveguide channel number.

efficiency with the proper choices of waveguide mode filter and fiber type. To be specific, the $3.5\text{-}\mu\text{m}$ -wide mode filter is designed for the coupling of the 1550-nm wave between the RPE waveguides and PM1550 fiber, while for the coupling of the 863-nm wave in DFG, the optimal mode-filter width is approximately $2.5\ \mu\text{m}$ and the better-matched fiber type is HI780. Although the multichannel DFG chips should be further customized when applied for long-distance multimode quantum memory, the present experiment undoubtedly proves the principle.

III. MULTICHANNEL UP-CONVERSION SPD

In the following, we show experiments with the 30-channel up-conversion SPD based on the packaged and integrated PPLN device. Note that the four side channels with much lower conversion efficiencies are excluded in this test. Figure 4 shows the setup for the single-photon detection test [8], in which only one channel of the chip is employed for simplicity and clarity. A single-frequency fiber laser fixed at $1950\ \text{nm}$ serves as the pump source. To correctly measure the detection efficiency, a single-photon source (SPS) consisting of two variable optical attenuators (VOAs) and a $99:1$ beam splitter is employed to provide 1×10^6 PM photons at $1550\ \text{nm}$. A calibrated power meter (Keysight 81634B) is utilized to monitor the input signal power and to ensure the correct signal-photon count. The SPS and the pump beam are combined with a $1550\text{-nm}/1950\text{-nm}$ WDM and launched into one channel of the fiber arrays at the input port of the PPLN waveguides. The employment of PM fiber components for both the pump and the signal improves the stability of the whole system.

To filter the noise photons generated from the pump laser, the up-conversion photons generated from the waveguide pass through a fiber filter. The fiber filter consists of an aperture and two band-pass filters with a combined bandwidth of $0.5\ \text{nm}$. The noise photons mainly come from the spontaneous Raman-scattering noise, parasitic noise caused by imperfect periodic poling structures, and second- and third-harmonic generation of the pump.

The remaining photons are detected by a silicon APD with a detection efficiency of 55% and an intrinsic noise of $60\ \text{counts/s}$.

We tune the pump power of every channel to achieve the maximum detection efficiency (DE). The system DE is obtained by dividing the number of detected count rate after noise-count-rate (NCR) subtraction by 1×10^6 , which is the signal-photon count rate before entering the WDM. DEs and NCRs for all the channels are shown in Fig. 5. The NCR contains the silicon APD's intrinsic noise.

The average DE and NCR of the middle 30 channels are 23.2% and $557\ \text{counts/s}$, respectively. The standard deviations of the DE and NCR between different channels are 2.73% and $48\ \text{counts/s}$, respectively. The DE and NCR of each channel can be tuned by the pump power, so we can achieve total consistency over all 30 different channels by slightly adjusting the 1950-nm pump power in each channel with a VOA. The insertion losses of the WDM and the filter are $0.5\ \text{dB}$ and $0.8\ \text{dB}$, respectively. The DEs measured here match with the data in Fig. 3, which are tested using milliwatt signal power when losses in the detection path are taken into account.

Optical isolation (OI) between nearby channels is important for a multichannel single-photon detector. To measure the OI, a 1550-nm signal is launched into one channel with the pump laser off and the leakage signal coupled into an adjacent channel $127\ \mu\text{m}$ away is up converted with the pump laser on and detected by Si APD. The measured OI between adjacent channels is $> 71\ \text{dB}$ for a waveguide center-to-center spacing of $127\ \mu\text{m}$. Compared with the best reported telecom-band SPD array, the superconducting SPD array, which has a DE of approximately 23% and a NCR of approximately $200\ \text{counts/s}$, our up-conversion SPD array may have more extensive applications because the superconducting SPD array suffers from considerable crosstalk due to the leakage current to the adjacent channels, resulting in a deteriorated signal-to-noise ratio [29,30].

Earlier in this paper, we propose a device of 60 channels with a waveguide center-to-center spacing of $63\ \mu\text{m}$.

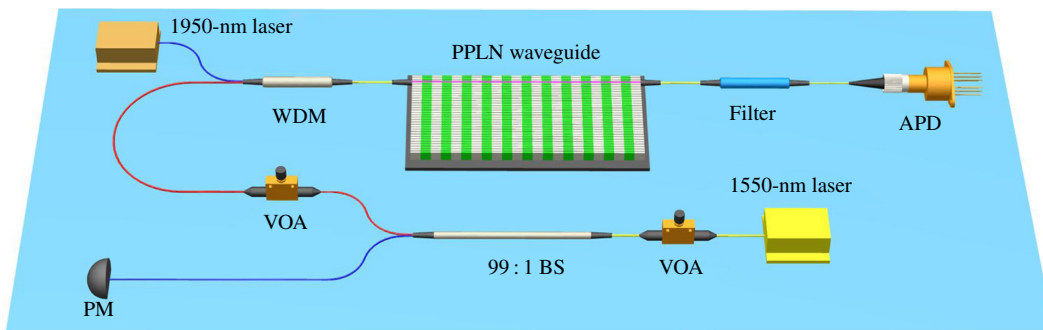


FIG. 4. A schematic of up-conversion SPD based on the 34-channel PPLN waveguide. VOA, variable optical attenuator; BS, beam splitter; APD, avalanche photodiode.

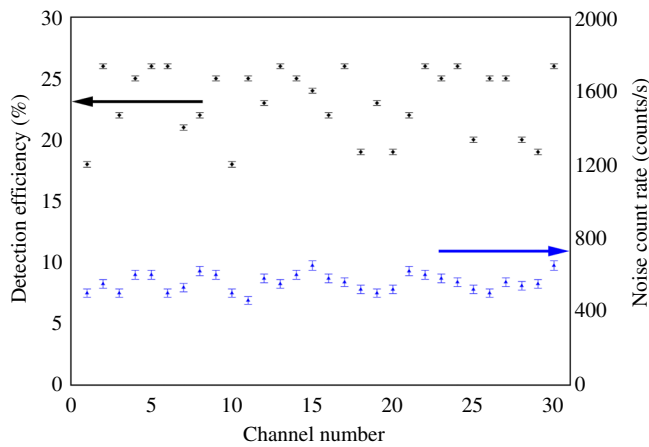


FIG. 5. The measured detection efficiency (black parallelogram) and dark-count rate (blue triangle) versus the waveguide channel number. The error bars denote the shot noises. Note the similarity between the detection efficiency here and the conversion efficiency in Fig. 3, with a ratio of 40% between them caused by losses in the detection path.

Without a fiber array with smaller core spacing for direct measurement of the SFG output, the OI for smaller channel spacing can be theoretically estimated using the isolation properties at the signal wavelength, because the conversion efficiencies of the waveguides are uniform. The logarithm of the OI has a linear relation to the distance between two faraway parallel waveguides [31]; therefore, the OI for waveguide center-to-center spacing of $63 \mu\text{m}$ can be deduced from those for waveguide center-to-center spacing of $50 \mu\text{m}$ and $127 \mu\text{m}$, which are available for measurement. From the measurements, we estimate that the OI of the 60-channel single-photon detector is $> 50 \text{ dB}$, much higher than the typical industrial standard of 30 dB . Limited by -30-dB crosstalk between adjacent channels, the maximum number of channels with a 5.5-mm -wide chip is approximately 120, which then needs a dense fiber array with a core-core spacing of only $30 \mu\text{m}$: this is not yet commercially available.

IV. CONCLUSIONS

In summary, an integrated photonic chip for multichannel QFCs based on an RPE PPLN waveguide is demonstrated. The input and output ports of the integrated chip are fiber coupled, with two fiber arrays to realize a convenient interface and improve the robustness of the device. The packaged optical circuits show uniform and excellent SFG conversion efficiencies for the different channels. Based on the same integrated chip, a demonstrative multichannel DFG experiment is carried out, showing that the integrated frequency-conversion chips could play a crucial role for long-distance multimode quantum memory [22–28]. Moreover, as a key component, the integrated chip is

used to build a multichannel telecom-band up-conversion single-photon detector. For the detector, an average detection efficiency of 23.2% and a noise count rate of 557 counts/s are achieved, with a standard deviation of 2.73% and 48 counts/s between 30 adjacent channels, as well as an ultrahigh optical isolation between nearby channels of more than 71 dB. This detector may find immediate applications in fields such as free-space laser communications, quantum-key distribution by WDM, and direct and non-line-of-sight single-photon imaging without scanning.

ACKNOWLEDGMENTS

This work was supported by the National Key R&D Program of China (Grants No. 2018YFB0504300, No. 2017YFA0303902, and No. 2017YFA0304000); the Key R&D Plan of Shandong Province (Grant No. 2019JZZY010205); the Natural Science Foundation of Shandong Province (Grant No. ZR2019LLZ003); the Chinese Academy of Science; the SAICT Experts Program; the Taishan Scholar Program of Shandong Province; the Quancheng Industrial Experts Program; and the 5150 Program for Talents Introduction.

-
- [1] J. Huang and P. Kumar, Observation of Quantum Frequency Conversion, *Phys. Rev. Lett.* **68**, 2153 (1992).
 - [2] S. Tanzilli, W. Tittel, M. Halder, O. Alibart, P. Baldi, N. Gisin, and H. Zbinden, A photonic quantum information interface, *Nature (London)* **437**, 116 (2005).
 - [3] C. Langrock, E. Diamanti, R. V. Roussev, Y. Yamamoto, M. M. Fejer, and H. Takesue, Highly efficient single-photon detection at communication wavelengths by use of upconversion in reverse-proton-exchanged periodically poled LiNbO_3 waveguides, *Opt. Lett.* **30**, 1725 (2005).
 - [4] L. Ma, O. Slattery, and X. Tang, Experimental study of high sensitivity infrared spectrometer with waveguide-based up-conversion detector, *Opt. Express* **17**, 14395 (2009).
 - [5] J. S. Pelc, L. Ma, C. R. Phillips, Q. Zhang, C. Langrock, O. Slattery, X. Tang, and M. M. Fejer, Long-wavelength-pumped upconversion single-photon detector at 1550 nm: Performance and noise analysis, *Opt. Express* **19**, 21445 (2011).
 - [6] L. Ma, O. Slattery, and X. Tang, Single photon frequency up-conversion and its applications, *Phys. Rep.* **521**, 69 (2012).
 - [7] G.-L. Shentu, J. S. Pelc, X.-D. Wang, Q.-C. Sun, M.-Y. Zheng, M. M. Fejer, Q. Zhang, and J.-W. Pan, Ultralow noise up-conversion detector and spectrometer for the telecom band, *Opt. Express* **21**, 13986 (2013).
 - [8] F. Ma, L.-Y. Liang, J.-P. Chen, Y. Gao, M.-Y. Zheng, X.-P. Xie, H. Liu, Q. Zhang, and J.-W. Pan, Upconversion single-photon detectors based on integrated periodically poled lithium niobate waveguides, *J. Opt. Soc. Am. B* **35**, 2096 (2018).

- [9] Y. Liu, T.-Y. Chen, L.-J. Wang, H. Liang, G.-L. Shentu, J. Wang, K. Cui, H.-L. Yin, N.-L. Liu, L. Li, X. Ma, J. S. Pelc, M. M. Fejer, C.-Z. Peng, Q. Zhang, and J.-W. Pan, Experimental Measurement-Device-Independent Quantum Key Distribution, *Phys. Rev. Lett.* **111**, 130502 (2013).
- [10] S.-K. Liao, H.-L. Yong, C. Liu, G.-L. Shentu, D.-D. Li, J. Lin, H. Dai, S.-Q. Zhao, B. Li, J.-Y. Guan, W. Chen, Y.-H. Gong, Y. Li, J.-G. Ren, Q. Zhang, C.-Z. Peng, and J.-W. Pan, Long-distance free-space quantum key distribution in daylight towards inter-satellite communication, *Nat. Photonics* **11**, 509 (2017).
- [11] M. Afzelius, C. Simon, H. de Riedmatten, and N. Gisin, Multimode quantum memory based on atomic frequency combs, *Phys. Rev. A* **79**, 052329 (2009).
- [12] R. Ikuta, Y. Kusaka, T. Kitano, H. Kato, T. Yamamoto, M. Koashi, and N. Imoto, Wide-band quantum interface for visible-to-telecommunication wavelength conversion, *Nat. Commun.* **2**, 537 (2011).
- [13] K. De Greve, L. Yu, P. L. McMahon, J. S. Pelc, C. M. Natarajan, N. Y. Kim, E. Abe, S. Maier, C. Schneider, M. Kamp, S. Höfling, R. H. Hadfield, A. Forchel, M. M. Fejer, and Y. Yamamoto, Quantum-dot spin-photon entanglement via frequency downconversion to telecom wavelength, *Nature (London)* **491**, 421 (2012).
- [14] N. Maring, P. Farrera, K. Kutluer, M. Mazzera, G. Heinze, and H. de Riedmatten, Photonic quantum state transfer between a cold atomic gas and a crystal, *Nature (London)* **551**, 485 (2017).
- [15] Y. Yu, F. Ma, X.-Y. Luo, B. Jing, P.-F. Sun, R.-Z. Fang, C.-W. Yang, H. Liu, M.-Y. Zheng, X.-P. Xie, W.-J. Zhang, L.-X. You, Z. Wang, T.-Y. Chen, Q. Zhang, X.-H. Bao, and J.-W. Pan, Entanglement of two quantum memories via fibres over dozens of kilometres, *Nature (London)* **578**, 240 (2020).
- [16] T. van Leent, M. Bock, R. Garthoff, K. Redeker, W. Zhang, T. Bauer, W. Rosenfeld, C. Becher, and H. Weinfurter, Long-Distance Distribution of Atom-Photon Entanglement at Telecom Wavelength, *Phys. Rev. Lett.* **124**, 010510 (2020).
- [17] H. Takesue, Erasing Distinguishability Using Quantum Frequency Up-Conversion, *Phys. Rev. Lett.* **101**, 173901 (2008).
- [18] L.-Y. Qu, J. Cotler, F. Ma, J.-Y. Guan, M.-Y. Zheng, X. Xie, Y.-A. Chen, Q. Zhang, F. Wilczek, and J.-W. Pan, Color Erasure Detectors Enable Chromatic Interferometry, *Phys. Rev. Lett.* **123**, 243601 (2019).
- [19] D. Shin, F. Xu, D. Venkatraman, R. Lussana, F. Villa, F. Zappa, V. Goyal, F. Wong, and J. Shapiro, Photon-efficient imaging with a single-photon camera, *Nat. Commun.* **7**, 12046 (2016).
- [20] M. O'Toole, D. B. Lindell, and G. Wetzstein, Confocal non-line-of-sight imaging based on the light-cone transform, *Nature (London)* **555**, 338 (2018).
- [21] X. Liu, I. Guillén, M. La Manna, J. H. Nam, S. A. Reza, T. H. Le, A. Jarabo, D. Gutierrez, and A. Velten, Non-line-of-sight imaging using phasor-field virtual wave optics, *Nature (London)* **572**, 620 (2019).
- [22] H.-N. Dai, H. Zhang, S.-J. Yang, T.-M. Zhao, J. Rui, Y.-J. Deng, L. Li, N.-L. Liu, S. Chen, X.-H. Bao, X.-M. Jin, B. Zhao, and J.-W. Pan, Holographic Storage of Biphoton Entanglement, *Phys. Rev. Lett.* **108**, 210501 (2012).
- [23] N. Sinclair, E. Saglamyurek, H. Mallahzadeh, J. A. Slater, M. George, R. Ricken, M. P. Hedges, D. Oblak, C. Simon, W. Sohler, and W. Tittel, Spectral Multiplexing for Scalable Quantum Photonics Using an Atomic Frequency Comb Quantum Memory and Feed-Forward Control, *Phys. Rev. Lett.* **113**, 053603 (2014).
- [24] M. Gündoğan, P. M. Ledingham, K. Kutluer, M. Mazzera, and H. de Riedmatten, Solid State Spin-Wave Quantum Memory for Time-Bin Qubits, *Phys. Rev. Lett.* **114**, 230501 (2015).
- [25] C. Laplane, P. Jobez, J. Etesse, N. Gisin, and M. Afzelius, Multimode and Long-Lived Quantum Correlations between Photons and Spins in a Crystal, *Phys. Rev. Lett.* **118**, 210501 (2017).
- [26] K. Kutluer, M. Mazzera, and H. de Riedmatten, Solid-State Source of Nonclassical Photon Pairs with Embedded Multimode Quantum Memory, *Phys. Rev. Lett.* **118**, 210502 (2017).
- [27] Y.-F. Pu, N. Jiang, W. Chang, H.-X. Yang, C. Li, and L.-M. Duan, Experimental realization of a multiplexed quantum memory with 225 individually accessible memory cells, *Nat. Commun.* **8**, 15359 (2017).
- [28] W. Chang, C. Li, Y.-K. Wu, N. Jiang, S. Zhang, Y.-F. Pu, X.-Y. Chang, and L.-M. Duan, Long-Distance Entanglement between a Multiplexed Quantum Memory and a Telecom Photon, *Phys. Rev. X* **9**, 041033 (2019).
- [29] E. E. Wollman, V. B. Verma, A. E. Lita, W. H. Farr, M. D. Shaw, R. P. Mirin, and S. W. Nam, Kilopixel array of superconducting nanowire single-photon detectors, *Opt. Express* **27**, 35279 (2019).
- [30] M. S. Allman, V. B. Verma, M. Stevens, T. Gerrits, R. D. Horansky, A. E. Lita, F. Marsili, A. Beyer, M. D. Shaw, D. Kumor, R. Mirin, and S. W. Nam, A near-infrared 64-pixel superconducting nanowire single photon detector array with integrated multiplexed readout, *Appl. Phys. Lett.* **106**, 192601 (2015).
- [31] N. Ortega-Quijano, F. Fanjul-Vélez, and J. L. Arce-Diego, Optical crosstalk influence in fiber imaging endoscopes design, *Opt. Commun.* **283**, 633 (2010).